



Interfacial electronic modulation by Fe₂O₃/NiFe-LDHs heterostructures for efficient oxygen evolution at high current density

Cheng-Fei Li^b, Ling-Jie Xie^b, Jia-Wei Zhao^b, Lin-Fei Gu^b, Jin-Qi Wu^b, Gao-Ren Li^{a,*}

^a College of Materials Science and Engineering, Sichuan University, Chengdu 610065, China

^b School of Chemistry, Sun Yat-Sen University, Guangzhou 510275, China

ARTICLE INFO

Keywords:

NiFe LDHs

Electronic modulation

Fe₂O₃

Oxygen evolution

Industrial current density

ABSTRACT

Designing and fabricating well-defined heterointerface catalysts with high electrocatalytic performance for oxygen evolution reaction (OER) at the industrial grade current density still remains a huge challenge. Here the flower-like nanosheets with rich Fe₂O₃/NiFe-layered double hydroxides (LDHs) heterointerfaces were fabricated, and they exhibit superior catalytic activity with a very low overpotential of 220 mV for OER at the industrial grade current density of 500 mA cm⁻² and fast reaction kinetics with a small Tafel slope of 32 mV dec⁻¹. Based on the analyses of operando Raman spectra, DFT theoretical calculations and electrochemical characterizations, the superior electrocatalytic performance of catalysts for OER at the industrial grade current density can be attributed to Fe₂O₃/NiFe-LDHs heterointerfaces that can obviously promote interfacial electron transfer from Ni²⁺ to Fe³⁺ and optimize d-orbit electronic configuration with e_g occupancy of Ni close to the unity, resulting in moderate adsorption/desorption energies of oxygenated intermediates, and thus facilitating remarkably electrocatalytic performance and superior intrinsic kinetics for OER in alkaline media.

1. Introduction

Water electrolysis is one of the most attractive routes for alleviating energy crisis and environmental pollution [1,2]. However, oxygen evolution reaction (OER) has been regarded as the bottleneck half-reaction for water splitting as it involves multistep proton-coupled electron transfer with high-energy barriers and suffers from a kinetically sluggish process [3]. In addition, for the general OER catalysts, with the increase of current density, especially at the industrial current density, the overpotential will increase significantly, resulting in rapid decrease of catalytic activity for OER. To realize the industrial application, developing highly efficient and robust OER catalysts for water electrolysis is a critical step. Recently, state-of-the-art IrO₂ and RuO₂ catalysts have been considered as the highly active catalysts for OER, however, their high cost and sluggish kinetics reaction at high current density greatly limited their widespread applications on a large scale [4,5]. Therefore, it is urgent to rationally design high-performance non-noble catalysts with fast reaction kinetics for efficient oxygen evolution at industrial grade current density.

Recently, the typical Fe/Ni-based composite catalysts are becoming potential candidates for OER due to their theoretically high

electrocatalytic activity as well as their low cost, which stimulate the ongoing exploration and optimization of cheap catalysts [6–8]. For the various solutions to develop OER catalysts, the most important strategy is the regulation of electronic structure of catalyst to optimize the binding energy of intermediates, which can be determined by e_g filling [9,10]. For example, Yang et al. [11] reported that the adsorption performance of intermediate was improved by e_g filling of surface transition metal cations to enhance the catalytic performance of metal oxides, which proved that e_g filling of catalytic active center was crucial to improve the kinetic slow reaction. Recently, there are also great interests in interface engineering [12], heteroatom doping [13] and vacancy/-strain/other defected structure [14–17] because they can provide a promising avenue to accelerate catalytic kinetics by regulating electronic structure (electrons in e_g and t_g orbitals) to optimize the binding energy of reaction intermediate. For example, Li group [18] reported an evident improvement of OER activity via the regulation of numerous electrons in e_g orbital after incorporating Fe and V into nickel hydroxide lattices. Baker et al. designed a superior active surface (Ni(OH)³⁺ and Co(OH)^{(3-δ)+}) supported on a highly electrically conductive FeNiCo₂O₄ core, where the e_g occupancy is close to 1, demonstrating the superior catalytic activity for OER in alkaline media [19]. However, the sluggish

* Corresponding author.

E-mail addresses: ligaoren@scu.edu.cn, ligaoren@mail.sysu.edu.cn (G.-R. Li).

<https://doi.org/10.1016/j.apcatb.2022.121097>

Received 6 November 2021; Received in revised form 17 December 2021; Accepted 9 January 2022

Available online 13 January 2022

0926-3373/© 2022 Elsevier B.V. All rights reserved.

kinetics of catalyst at the industrial current density still remains a huge challenge because of strong binding of oxygen-containing intermediates on the electroactive site, which seriously hampers OER catalytic performance enhancement [20–22].

Based on the aforementioned merits and challenging issues, herein, we synthesized $\text{Fe}_2\text{O}_3/\text{NiFe-LDHs}$ composite catalysts with a high density of atomically matched heterointerfaces by one-step hydrothermal method. Physical characterizations verify that the Fe_2O_3 could promote interface electron transfer from Ni^{2+} to Fe^{3+} , indicating that the e_g and t_g orbitals filling can be effectively modulated to optimize the adsorption-desorption behaviors of intermediates, evidenced by the in-situ Raman spectra and theoretical calculations. $\text{Fe}_2\text{O}_3/\text{NiFe-LDHs}$ exhibits high catalytic activity with a very low overpotential of 220 mV for OER at an industrial grade current density of 500 mA cm^{-2} and ultrafast reaction kinetics with a small Tafel value of 32 mV dec^{-1} . Our work not only provides a new route for the design of bimetallic layered double hydroxides with superior catalytic performance for OER at industrial grade current density, but also enlightens the fundamental understanding of electronic structure-catalytic activity relationship.

2. Experimental section

2.1. Syntheses of $\text{Fe}_2\text{O}_3/\text{NiFe-LDHs}$

Firstly, the commercial Ni foam (NF) ($2.8 \text{ cm} \times 3 \text{ cm} \times 1 \text{ mm}$) was successively washed in acetone and dilute HCl solution ($V_{\text{H}_2\text{O}}: V_{\text{HCl}}=1:2$) under ultrasonication for 30 min and 20 min, respectively. After cleaning with water, the NF was transferred into 12 mL of solution (0.48 mmol $\text{FeCl}_3 \cdot 6 \text{ H}_2\text{O}$, 0.75 mL water, 0.75 mL ethanol, 10 mL N,N-dimethylformamide (DMF), 1.2 g saccharin) in 25 mL Teflon-lined autoclave. Then, the autoclave was sealed and maintained at 125°C for 12 h in an oven. The brown red $\text{Fe}_2\text{O}_3/\text{NiFe-LDHs}$ grown on NF was taken out after naturally cooling down to room temperature, and washed with deionized H_2O . Finally, the $\text{Fe}_2\text{O}_3/\text{NiFe-LDHs}$ was dried under room temperature for further characterizations.

2.2. Syntheses of Fe_2O_3

A mixed solution of 0.48 mmol $\text{FeCl}_3 \cdot 6 \text{ H}_2\text{O}$, 0.75 mL water, 0.75 mL ethanol, 1.2 g saccharin and 10 mL N,N-dimethylformamide (DMF) was ultrasonicated for 30 min and then was transferred into 25 mL Teflon-lined autoclave. The autoclave was sealed and maintained at 125°C for 12 h in an oven. Finally, the brown red Fe_2O_3 was achieved after naturally cooling down to room temperature, washed with deionized H_2O and dried at 65°C . For electrode preparation, 2 mg of commercial Fe_2O_3 were ultrasonically dispersed in mixed solution containing 895 μL of ethanol, 100 μL of water and 5 μL of 5 wt% nafion. After that, 150 μL ink were deposited on a piece of clean NF ($1 \text{ cm} \times 0.5 \text{ cm} \times 1 \text{ mm}$) and dried by the evaporation at room temperature.

2.3. Syntheses of RuO_2

2 mg of commercial RuO_2 was ultrasonically dispersed in solution of 895 μL ethanol, 100 μL water and 5 μL 5 wt% nafion. After that, 150 μL the ink was deposited on a piece of clean NF ($1 \text{ cm} \times 0.5 \text{ cm} \times 1 \text{ mm}$) and dried by the evaporation at room temperature.

2.4. Syntheses of NiFe-LDHs

In a typical process, 0.48 mmol $\text{Fe}(\text{NO}_3)_3 \cdot 4 \text{ H}_2\text{O}$, 1.44 mmol $\text{Ni}(\text{NO}_3)_2 \cdot 6 \text{ H}_2\text{O}$, 3 mmol urea, and 3 mmol NH_4F were dissolved in 30 mL of H_2O , and then was transferred into a 45 mL Teflon-lined autoclave containing the cleaned NF. Finally, the Teflon-lined autoclave was sealed and heated at 150°C for 3 h in an oven. After cooling down to room temperature naturally, the resulting $\text{NiFe-LDHs}/\text{NF}$ was rinsed with deionized water and then was dried at 70°C for further use.

2.5. Materials characterizations

Transmission electron microscopy (FESEM, FEI Sirion-200), Field emission scanning electron microscopy (FEI TECNAI F30 TEM with an acceleration voltage of 300 kV) and X-ray powder diffraction (Rigaku D/Max 2550 X-ray diffractometer using $\text{Cu K}\alpha$ radiation ($\lambda = 1.54178 \text{ \AA}$)) were employed to characterize the morphologies and phase of as-prepared samples. X-Ray photoelectron spectroscopy (XPS) using an ESCAKAB 250 X-Ray photoelectron spectrometer was carried out to study the chemical compositions of as-prepared samples. Raman spectra were acquired on a laser microRaman spectrometer (Renishaw inVia) equipped with a He-Ne laser (wavelength = 532 nm).

2.6. Apparatus for in-situ Raman spectroscopy and electrochemistry

A especial self-built cell includes: the synthesized samples as working electrode, a graphite rod as the counter electrode, and a saturated Hg/HgO electrode as the reference electrodes. The objective of Raman device was coated by the Teflon film with a thickness of 0.025 mm to avoid the corrosion in 0.1 M KOH electrolyte. In situ Raman spectra of the electrodes were acquired on a laser microRaman spectrometer with 0.5 mW of 532 nm laser excitation.

2.7. Electrochemical measurements

All the electrochemical tests were carried out using an electrochemical station (Shanghai Chenhua Instrument Co. Ltd.) with a conventional three-electrode system, including saturated Hg/HgO electrode as reference electrode, carbon rod as counter electrode and as-prepared samples as working electrode. The linear sweep voltammetry (LSV) was conducted at a scan rate of 2 mV s^{-1} in 1.0 M KOH. All polarization curves were corrected for ohmic-drop compensation. The EIS measurements were conducted in a frequency range from 100 KHz to 10 mHz with an AC amplitude of 0.55, 0.6, 0.65 and 0.7 V vs. Hg/HgO . The chronoamperometry was employed to characterize the stability of as-prepared electrode with same geometric area (1.0 cm^2). To measure electrochemical double-layer capacitance (C_{dl}), the potentials were swept at a range of no faradic process with six different scan rates (5, 10, 20, 30 and 40 mV s^{-1}). The C_{dl} derived from the slope of the linear fit from the measured capacitive current densities at the average potential in the selected range against the scan rate. The overall water splitting measurement in 1.0 M KOH was carried out in a two-electrode system using RuO_2 or $\text{Fe}_2\text{O}_3/\text{NiFe-LDHs}$ (on Ni foam) as anode, and 20 wt% Pt/C (on Ni foam) as cathode. The electrochemical active surface area (ECSA) is calculated according to the following equation.

$$ECSA = \frac{C_{dl}}{40 \mu\text{F cm}^{-2}}$$

2.8. MEA electrolyser

A membrane electrode assembly (MEA) electrolysis cell with an anion exchange membrane was constructed (Fig. 5b in paper) to evaluate the performance of the as-prepared $\text{Fe}_2\text{O}_3/\text{NiFe-LDHs}$ catalyst. Specifically, the electrolyzer includes two end plates, on which a single serpentine flow field (4 cm^2 surface area, 1.0 mm width, 0.5 mm depth and 1.0 mm rib) was machined. $\text{Fe}_2\text{O}_3/\text{NiFe-LDHs}$ can be directly utilized as the anode ($2 \times 2 \text{ cm}^2 \times 2 \text{ mm}$). The cathode commercial Pt/C was prepared by dispersing 5.0 mg active catalyst in 950 μL ethanol with 50 μL 5 wt% Nafion solution under ultrasonication for 30 min. Then 800 μL of the above suspension was dropped onto a carbon paper ($2 \times 2 \text{ cm}^2 \times 1 \text{ mm}$) and left to dry with a fan. Therefore, the catalyst loading amount was 1 mg cm^{-2} . The anode commercial RuO_2 electrode was fabricated with the same procedure. For OER measurement, linear sweep voltammetry with scan rate of 5 mV s^{-1} was carried out at room temperature.

2.9. Computational methods

The Vienna Ab Initio Package (VASP) [23,24] was employed to perform all of the density functional theory (DFT) calculations within the generalized gradient approximation (GGA) using the PBE [25] formulation. The projected augmented wave (PAW) potential [26,27] was chosen to describe ionic cores and take valence electrons into account using a plane wave basis set with a kinetic energy cutoff of 400 eV. The partial occupancies of the Kohn-Sham orbitals were allowed using the Gaussian smearing method and a width of 0.05 eV. The electronic energy was considered self-consistent when the energy change was smaller than 10^{-4} eV. A geometry optimization was considered convergent when the force change was smaller than 0.05 eV/Å.

Grimme's DFT-D3 methodology [28] was used to describe the dispersion interactions. The vacuum spacing perpendicular to the plane of the structure is 15 Å. The Brillouin zone integral used the surfaces structures of $2 \times 2 \times 1$ monkhorst pack K point sampling. Finally, the adsorption energies (E_{ads}) are calculated as $E_{\text{ads}} = E_{\text{ad/sub}} - E_{\text{ad}} - E_{\text{sub}}$, where $E_{\text{ad/sub}}$, E_{ad} and E_{sub} are the optimized adsorbate/substrate system, the adsorbate in the structure and the clean substrate respectively. The free energy is calculated as follows:

$$G = E + \text{ZPE} - TS.$$

where G , E , ZPE and TS are the free energy, total energy from DFT calculations, zero point energy and entropic contributions, respectively.

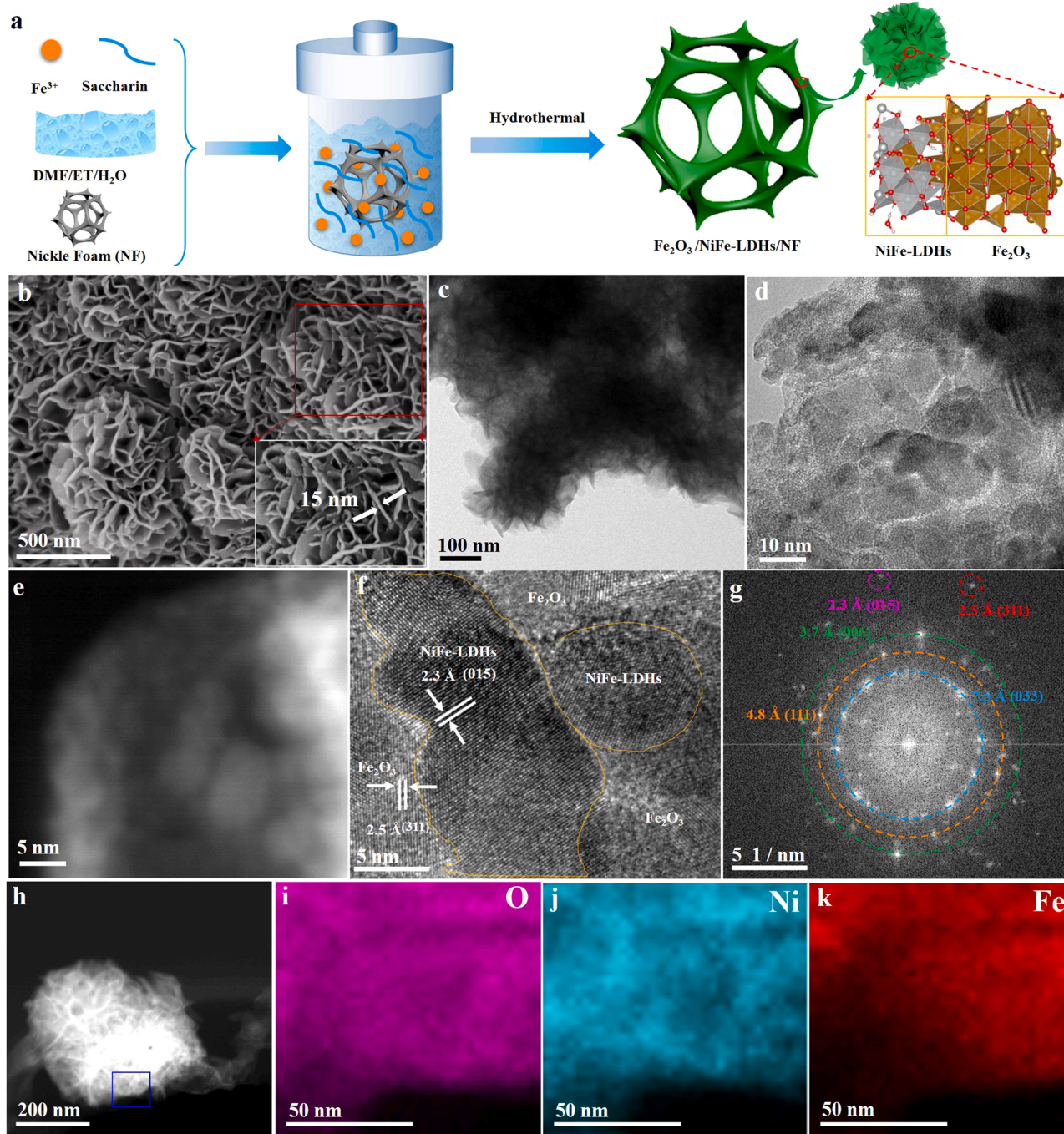


Fig. 1. a) Schematic illustration of the synthetic process of Fe₂O₃/NiFe-LDHs; b) SEM image; c-d) TEM images; e) HAADF-STEM image; f) HRTEM image; g) FFT pattern; h) HAADF-STEM image; and i-k) STEM-EDS mappings of Fe₂O₃/NiFe-LDHs.

3. Results and discussion

Here a one-step experimental procedure was utilized to synthesize $\text{Fe}_2\text{O}_3/\text{NiFe-LDHs}$ with atomically matched heterointerfaces by using nickel foam (NF) as conductive substrate and nickel source, ferric chloride as iron source and saccharin as surface-active agent. The schematic illustration of the synthesis of $\text{Fe}_2\text{O}_3/\text{NiFe-LDHs}$ is shown in Fig. 1a. As shown in SEM image in Fig. 1b, $\text{Fe}_2\text{O}_3/\text{NiFe-LDHs}$ consisted of flower-like 3-dimensional (3D) ultrathin nanosheets with an average thickness of ~ 15 nm, which is beneficial for the desorption of gas bubbles and will promote mass transfer process [29,30]. To confirm the catalysts are comprised of Fe_2O_3 and NiFe-LDHs, their crystal structures were confirmed by X-ray diffraction (XRD) pattern and Raman pattern. The characteristic peaks of $\text{Fe}_2\text{O}_3/\text{NiFe-LDHs}$ in Fig. S1 are well matched with standard Fe_2O_3 (JCPDS No. 39-1346) and NiFe-LDHs (JCPDS No. 49-0188). The Raman spectrum further reveals the existence of $\text{Fe}_2\text{O}_3/\text{NiFe-LDHs}$ as shown in Fig. S2, which shows the characteristic peaks (~ 475 and ~ 530 cm^{-1}) of NiFe-LDHs [31], and the vibrational bands at ~ 210 , 320 and 691 cm^{-1} in low wavenumber region can be ascribed to the characteristic peaks of Fe_2O_3 [32,33]. The transmission electron microscopy (TEM) images in Fig. 1c–d show 3D nanosheets are consisted of nanoparticles with 5–15 nm in diameters. Interestingly, high-resolution TEM (HRTEM) image in Fig. 1f shows a high density of heterointerfaces, where NiFe-LDHs with (015) nanofacets are intimately contacted with Fe_2O_3 with (311) facets. The fast Fourier transformation image in Fig. 1g confirms the presence of various lattice planes, consisted with the XRD results of $\text{Fe}_2\text{O}_3/\text{NiFe-LDHs}$. Moreover, the elemental mapping analysis shows that the Ni, Fe and O elements are distributed evenly throughout the selected area as shown in Fig. 1i–k. The inductively coupled plasma atomic emission spectroscopy (ICP-AES) analysis shows the atomic ratio of Fe/Ni is about 35.5% in $\text{Fe}_2\text{O}_3/\text{NiFe-LDHs}$. Combining with thermogravimetric analysis, the weight percentage of Fe_2O_3 in the $\text{Fe}_2\text{O}_3/\text{NiFe-LDHs}$ is calculated to be 64.5 wt% (Fig. S3). In this paper, the $\text{Fe}_2\text{O}_3/\text{NiFe-LDHs}$ with weight percentage of Fe_2O_3 of 64.5 wt% is mainly used to study sample

characterizations and OER catalytic performance.

Inspired by the above unique heterointerface structure and compositions, the electrocatalytic activity of $\text{Fe}_2\text{O}_3/\text{NiFe-LDHs}$ toward OER was evaluated with three-electrode system in solution of 1.0 M KOH. For the comparison studies, the Fe_2O_3 nanosheets loaded on NF and NiFe-LDHs grown on NF were also fabricated as shown in Figs. S4 and S5, respectively. The commercial RuO_2 loaded on NF with the same loading (0.3 mg cm^{-2}) was also fabricated. Fig. 2a shows iR-corrected linear sweep voltammetry (LSV) curves of $\text{Fe}_2\text{O}_3/\text{NiFe-LDHs}$, NiFe-LDHs, Fe_2O_3 and RuO_2 , and the $\text{Fe}_2\text{O}_3/\text{NiFe-LDHs}$ catalysts exhibit record high OER catalytic activity with a very low overpotential of only 220 mV at 500 mA cm^{-2} . Furthermore, when the current density was up to 800 mA cm^{-2} , the overpotential still is very low of only 236 mV, indicating that the $\text{Fe}_2\text{O}_3/\text{NiFe-LDHs}$ has excellent catalytic activity for OER at a high current density and can meet the industrial-scale application [34], and even outperform the best catalysts reported currently (Table S1). In sharp contrast to $\text{Fe}_2\text{O}_3/\text{NiFe-LDHs}$, three other catalysts NiFe-LDHs, Fe_2O_3 and RuO_2 show much lower OER catalytic activities ($\eta_{500} > 450$ mV), especially at a high current density. Surprisingly, the physically mixed $\text{Fe}_2\text{O}_3 + \text{NiFe-LDHs}$ also shows low OER catalytic activity (Fig. S6), such as a high overpotential of 438 mV at 100 mA cm^{-2} , large electrochemical impedance ($\sim 97 \Omega$), and large Tafel value (81 mV dec^{-1}) (Fig. S7). These facts clearly indicate that the atomically matched $\text{Fe}_2\text{O}_3/\text{NiFe-LDHs}$ heterointerfaces are crucial for superior electrocatalytic activity of OER.

It is well known that rapid reaction kinetics is an important factor for superior OER catalytic activity. Tafel slopes of various samples were further investigated as shown in Fig. 2b. As expected, the Tafel value of $\text{Fe}_2\text{O}_3/\text{NiFe-LDHs}$ is only 32 mV dec^{-1} , which is much lower than those of Fe_2O_3 (73 mV dec^{-1}), RuO_2 (87 mV dec^{-1}) and NiFe-LDHs (60 mV dec^{-1}), and is also lower than those of most of the reported catalysts (Table S1 and Fig. 2c), indicating the superiority of unique $\text{Fe}_2\text{O}_3/\text{NiFe-LDHs}$ heterointerface can obviously enhance OER reaction kinetics. In addition, the electrochemical impedance spectra (EIS) has been regarded as an important technology for the evaluation of electronic

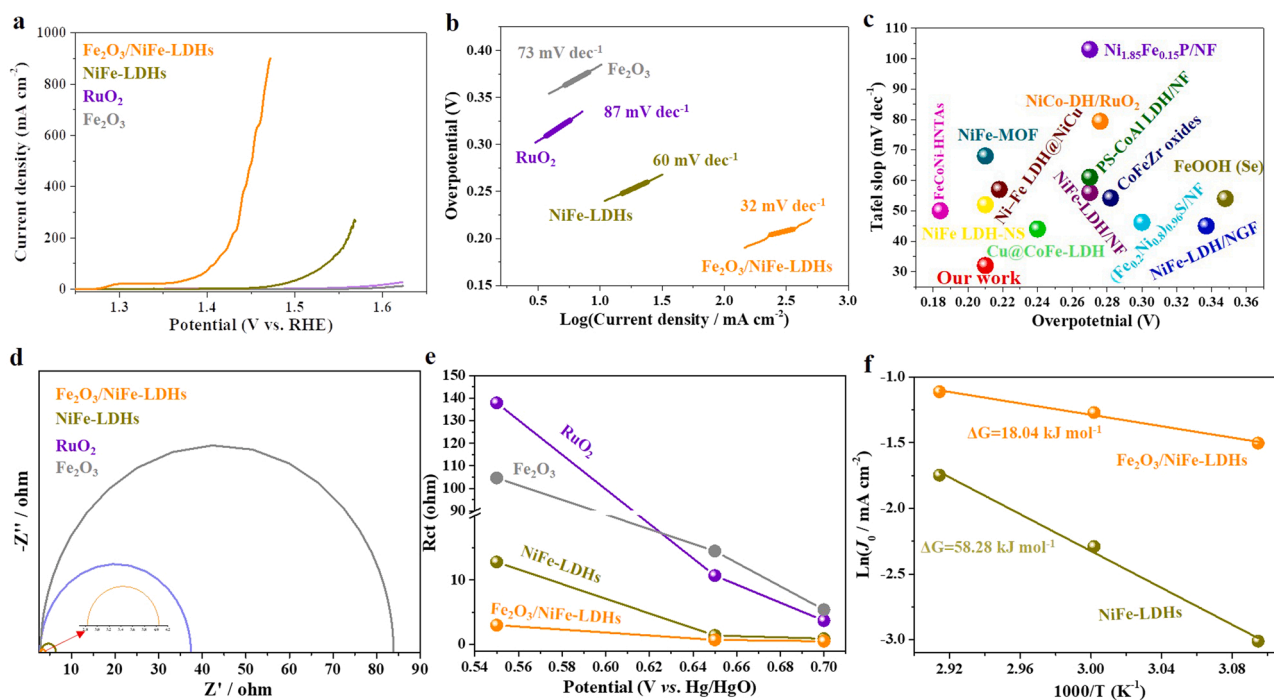


Fig. 2. a) iR-compensated polarization curves of $\text{Fe}_2\text{O}_3/\text{NiFe-LDHs}$, pure NiFe-LDHs, Fe_2O_3 and commercial RuO_2 catalyst; b) The corresponding Tafel plots of the above four catalysts; c) Comparisons of Tafel values and overpotential of $\text{Fe}_2\text{O}_3/\text{NiFe-LDHs}$ with the reported catalysts; d) The electrochemical impedance plots obtained at a potential of 0.6 V vs. Hg/HgO; e) Charge transfer resistance versus potential plots of the above four catalysts; f) Arrhenius plots of $\text{Fe}_2\text{O}_3/\text{NiFe-LDHs}$ and NiFe-LDHs.

transmission during OER reaction. The $\text{Fe}_2\text{O}_3/\text{NiFe-LDHs}$ shows the smallest charge transfer resistance ($1.2\ \Omega$) compared with NiFe-LDHs ($3.5\ \Omega$), commercial RuO_2 ($34.5\ \Omega$) and Fe_2O_3 ($81.1\ \Omega$) as shown in Fig. 2d, indicating the fastest electron transfer process in $\text{Fe}_2\text{O}_3/\text{NiFe-LDHs}$. To further investigate the reaction kinetics at different potentials by the in-situ measurement of electrical resistance during EIS process (Fig. S8–11). The obtained data from all samples are fitted with the corresponding equivalent circuit composed of electrolyte resistance (R_s) and charge-transfer resistance (R_{ct}) in parallel with the constant-phase element (CPE), and the results are shown in Table S2. It is evident that the charge transfer resistance of $\text{Fe}_2\text{O}_3/\text{NiFe-LDHs}$ decreases dramatically until stable with the applied potential increasing, but the other two catalysts still show large charge transfer resistance (Fig. 2e), suggesting that the $\text{Fe}_2\text{O}_3/\text{NiFe-LDHs}$ interfaces can efficiently promote electronic transmission for OER. In addition, the thermodynamic OER activation energy is calculated via Arrhenius plots as shown in Fig. 2f based on the exchange current density j_0 at the different temperatures derived from the Tafel curves and temperature-dependent LSVs (Figs. S12–S15) [35–37]. Notably, the activation energy of $\text{Fe}_2\text{O}_3/\text{NiFe-LDHs}$ is calculated to be $18.04\ \text{kJ mol}^{-1}$, which is only about 1/3 of that of NiFe-LDHs ($58.28\ \text{kJ mol}^{-1}$), suggesting a significant promotion of OER kinetics after the formation of $\text{Fe}_2\text{O}_3/\text{NiFe-LDHs}$.

To further understand the intrinsic activity of $\text{Fe}_2\text{O}_3/\text{NiFe-LDHs}$, the cyclic voltammetry (CV) curves at the different scan rates are measured (Fig. S16) and the electrochemical active surface area (ECSA) was calculated. We found that the $\text{Fe}_2\text{O}_3/\text{NiFe-LDHs}$ owned a high ECSA of $70.25\ \text{cm}^2$, which is much larger than those of NiFe-LDHs ($61.0\ \text{cm}^2$), RuO_2 ($22.75\ \text{cm}^2$) and Fe_2O_3 ($9.5\ \text{cm}^2$), suggesting that the $\text{Fe}_2\text{O}_3/\text{NiFe-LDHs}$ can expose more active sites. The LSVs in Fig. 2a were further normalized by C_{dl} as shown in Fig. S17, which indicates that the $\text{Fe}_2\text{O}_3/\text{NiFe-LDHs}$ has much higher intrinsic activity than NiFe-LDHs , Fe_2O_3 and RuO_2 catalysts.

The durability of $\text{Fe}_2\text{O}_3/\text{NiFe-LDHs}$ was also evaluated through chronopotentiometry experiments. As shown in Fig. S18, $\text{Fe}_2\text{O}_3/\text{NiFe-LDHs}$ catalysts exhibit superior stability with negligible degradation after galvanostatic electrolysis of 120 h at 10 and $20\ \text{mA cm}^{-2}$. To highlight the outstanding structural robustness and mechanical stability, the morphology of $\text{Fe}_2\text{O}_3/\text{NiFe-LDHs}$ after electrocatalytic stability test was also investigated. Figs. S19–S20 presents the typical Raman pattern, SEM and TEM images of $\text{Fe}_2\text{O}_3/\text{NiFe-LDHs}$ after long-term durability test, and the flower-like 3D structures and high density heterointerfaces of $\text{Fe}_2\text{O}_3/\text{NiFe-LDHs}$ were well maintained and no agglomeration of nanoparticles.

In order to further investigate the role of high density of heterointerfaces on enhancing electrocatalytic performance of $\text{Fe}_2\text{O}_3/\text{NiFe-LDHs}$, two different contents of Fe_2O_3 in $\text{Fe}_2\text{O}_3/\text{NiFe-LDHs}$ including 58.6 wt% and 82.2 wt% were prepared, and the corresponding catalysts are denoted as $\text{Fe}_2\text{O}_3/\text{NiFe-LDHs-58.6 wt\%}$ and $\text{Fe}_2\text{O}_3/\text{NiFe-LDHs-82.2 wt\%}$, respectively. With $\text{Fe}_2\text{O}_3/\text{NiFe-LDHs}$ molar ratio increasing, it can be seen that the thickness of nanosheet increases from 10 to 20 nm (Fig. S21), and the surface becomes rougher, but the heterointerfaces of $\text{Fe}_2\text{O}_3/\text{NiFe-LDHs-58.6 wt\%}$ and $\text{Fe}_2\text{O}_3/\text{NiFe-LDHs-82.2 wt\%}$ are inconspicuous as shown in Figs. S22–S23. The iR-corrected LSVs of $\text{Fe}_2\text{O}_3/\text{NiFe-LDHs-58.6 wt\%}$ and $\text{Fe}_2\text{O}_3/\text{NiFe-LDHs-82.2 wt\%}$ were measured, and they are shown in Fig. S24a, which shows that the $\text{Fe}_2\text{O}_3/\text{NiFe-LDHs-58.6 wt\%}$ and $\text{Fe}_2\text{O}_3/\text{NiFe-LDHs-82.2 wt\%}$ also display high OER catalytic activity with low overpotentials of 268 and 290 mV, respectively, at a high current density of $100\ \text{mA cm}^{-2}$. However, the overpotential of $\text{Fe}_2\text{O}_3/\text{NiFe-LDHs-64.5 wt\%}$ is still slightly smaller than those of $\text{Fe}_2\text{O}_3/\text{NiFe-LDHs-58.6 wt\%}$ and $\text{Fe}_2\text{O}_3/\text{NiFe-LDHs-82.2 wt\%}$ at $100\ \text{mA cm}^{-2}$ (Fig. 2a), and this can be attributed to higher density of atomically matched heterointerfaces in the $\text{Fe}_2\text{O}_3/\text{NiFe-LDHs-64.5 wt\%}$ than those in $\text{Fe}_2\text{O}_3/\text{NiFe-LDHs-58.6 wt\%}$ and $\text{Fe}_2\text{O}_3/\text{NiFe-LDHs-82.2 wt\%}$. In addition, the reaction kinetics of catalysts for OER were studied by Tafel slopes (Fig. S24b), and the $\text{Fe}_2\text{O}_3/\text{NiFe-LDHs-64.5 wt\%}$ owns the lowest Tafel value. So the above results show that the high

density heterointerfaces in $\text{Fe}_2\text{O}_3/\text{NiFe-LDHs-64.5 wt\%}$ with optimal percentage of Fe_2O_3 can obviously enhance OER catalytic performance. The electrochemical resistance spectra were utilized to study OER kinetics on catalysts as shown in Fig. S24c, which show larger charge transfer resistances of $\text{Fe}_2\text{O}_3/\text{NiFe-LDHs-58.6 wt\%}$ ($2.3\ \Omega$) and $\text{Fe}_2\text{O}_3/\text{NiFe-LDHs-82.2 wt\%}$ ($19.1\ \Omega$) than that of $\text{Fe}_2\text{O}_3/\text{NiFe-LDHs-64.5 wt\%}$ ($1.2\ \Omega$), suggesting a slow electron transfer during the electrochemical reaction.

To study the origin of high electrocatalytic performance of $\text{Fe}_2\text{O}_3/\text{NiFe-LDHs}$ for OER, the strong electronically coupled interactions and oxidation states are studied by X-ray photoelectron spectroscopy (XPS). The XPS analysis reveals that the composite catalysts contain Ni, Fe and O as the main elements. Furthermore, as displayed in Fig. 3a, Ni $2p_{3/2}$ peak ($856.4\ \text{eV}$) of $\text{Fe}_2\text{O}_3/\text{NiFe-LDHs}$ shifts towards higher binding energy by $\sim 0.7\ \text{eV}$ compared with that of NiFe-LDHs [38,39], indicating that the valence state of Ni cation increases via strong interfacial interaction after modifying with Fe_2O_3 . To analyze the role of interfacial Fe_2O_3 on the active species for OER, Ni oxidation state of $\text{Fe}_2\text{O}_3/\text{NiFe-LDHs}$ was studied after OER test. Noticeably, Ni^{3+} cations from NiOOH phase appear [40,41]. Additionally, the peak of $\text{Ni}^{3+}\ 2p_{3/2}$ obviously shifts toward positive value ($\text{Ni}^{3+}/\text{Ni}^{3+\delta}$), and the peak area of Ni^{3+} ions from $\text{Fe}_2\text{O}_3/\text{NiFe-LDHs}$ after OER is larger than that of post-OER NiFe-LDHs , indicating that the Fe_2O_3 can facilitate the formation of rich-high-valence Ni^{3+} on the surface of $\text{Fe}_2\text{O}_3/\text{NiFe-LDHs}$ that was mainly responsible for the active sites during OER [42]. The above phenomenon can be explained through the analysis of valence electron structures of metal ions in the $\text{Fe}_2\text{O}_3/\text{NiFe-LDHs}$ (Fig. 3b). The valence electron configuration of $\text{Ni}^{2+}\ 3d^8\ (t_{2g}^6 e_g^2)$ in low-spin state are fully occupied, which causes e^-e^- repulsion between the bridging O^{2-} and Ni^{2+} [43]. Whereas the three unpaired electrons in π -symmetry (t_{2g}) d-orbitals of $\text{Fe}^{3+}\ 3d^5\ (t_{2g}^3 e_g^2)$ interact with the bridging O^{2-} via π -donation [21,44]. Therefore, the coupling between Fe^{3+} and Ni^{2+} leads to partial electron transfer from Ni^{2+} to Fe^{3+} , resulting in the shift of $\text{Ni}^{2+}\ 2p$ peak of $\text{Fe}_2\text{O}_3/\text{NiFe-LDHs}$ to a higher binding energy. Here the superior catalytic activity of $\text{Fe}_2\text{O}_3/\text{NiFe-LDHs}$ can well be elucidated based on Yang's principles [14]. Namely, the numerous Ni^{3+} cations (octahedron) will bring an e_g occupancy of Ni closer to the unity as a high-activity configuration (Fig. 3c), which will be beneficial to oxygen evolution due to moderate metal-oxygen bond between metal cations and OER intermediates. This can be evidenced by in-situ Raman spectra as shown in Fig. 3d. Noticeably, the position of metal-OOH bond for $\text{Fe}_2\text{O}_3/\text{NiFe-LDHs}$ is lower than that of NiFe-LDHs , suggesting that the binding strength of oxygen-containing intermediates is optimized significantly, accelerating the sluggish OER kinetics [45]. Moreover, Fe $2p$ XPS peaks of $\text{Fe}_2\text{O}_3/\text{NiFe-LDHs}$ shifts to lower binding energy after introducing Fe_2O_3 because of the partial Ni-to-Fe electron transfer (Fig. 3e), indicating that the valence state of Fe in the hybrids is significantly reduced. It is worth mentioning that the presence of Fe^{2+} is due to the reaction between Fe^{3+} and NF ($2\text{Fe}^{3+} + \text{Ni} = 2\text{Fe}^{2+} + \text{Ni}^{2+}$) [46]. Furthermore, the high-resolution Fe^{3+} peak shows similar binding energy in post-OER $\text{Fe}_2\text{O}_3/\text{NiFe-LDHs}$ and post-OER NiFe-LDHs . But the ratio of $\text{Fe}^{3+}/\text{Fe}^{2+}$ in post-OER $\text{Fe}_2\text{O}_3/\text{NiFe-LDHs}$ (3.3) is much higher than that of post-OER NiFe-LDHs (2.6). This can be attributed to strong electronic interactions between NiFe-LDHs and Fe_2O_3 .

To further reveal the electrocatalytic mechanism experimentally, an operando Raman technology was employed. A series of Raman spectra of $\text{Fe}_2\text{O}_3/\text{NiFe-LDHs}$ were recorded at applied potentials ranging from 0.4 to 0.75 V in 0.1 M KOH electrolyte as shown in Fig. 3f, which shows only a broad shoulder peak ($400\text{--}600\ \text{cm}^{-1}$) until 0.5 V. When the applied potential reaches 0.6 V or higher, the peaks at 480 and $552\ \text{cm}^{-1}$ are observed, and they can be attributed to Ni-O vibrations of NiOOH intermediate from $\text{Fe}_2\text{O}_3/\text{NiFe-LDHs}$ [41,47], indicating NiFe-LDHs have been transformed into oxyhydroxides during oxygen evolution. The results of operando Raman spectra show that the NiOOH intermediate is active species for OER, which is consistent with XPS results.

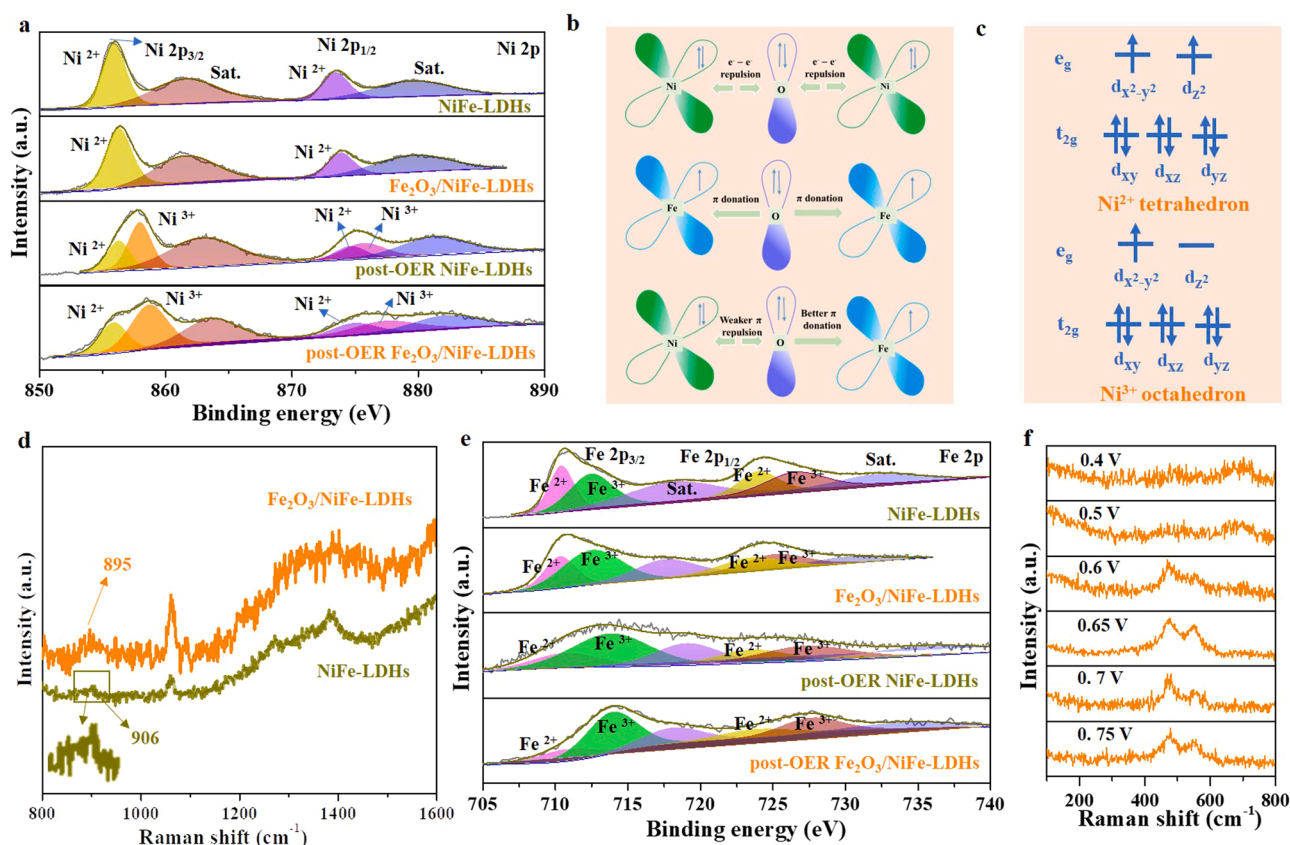


Fig. 3. a) Ni 2p XPS spectra of $\text{Fe}_2\text{O}_3/\text{NiFe-LDHs}$, NiFe-LDHs , $\text{post-OER Fe}_2\text{O}_3/\text{NiFe-LDHs}$ and $\text{post-OER NiFe-LDHs}$; b) Schematic representations of electronic coupling between Ni and Fe in $\text{Fe}_2\text{O}_3/\text{NiFe-LDHs}$; c) The electronic structure of a Ni ion at tetrahedral and octahedral sites; d) Operando Raman spectra of $\text{Fe}_2\text{O}_3/\text{NiFe-LDHs}$ and NiFe-LDHs ; e) Fe 2p XPS spectra of $\text{Fe}_2\text{O}_3/\text{NiFe-LDHs}$, NiFe-LDHs , $\text{post-OER Fe}_2\text{O}_3/\text{NiFe-LDHs}$ and $\text{post-OER NiFe-LDHs}$; f) Operando Raman spectra of $\text{Fe}_2\text{O}_3/\text{NiFe-LDHs}$ under the different applied potentials.

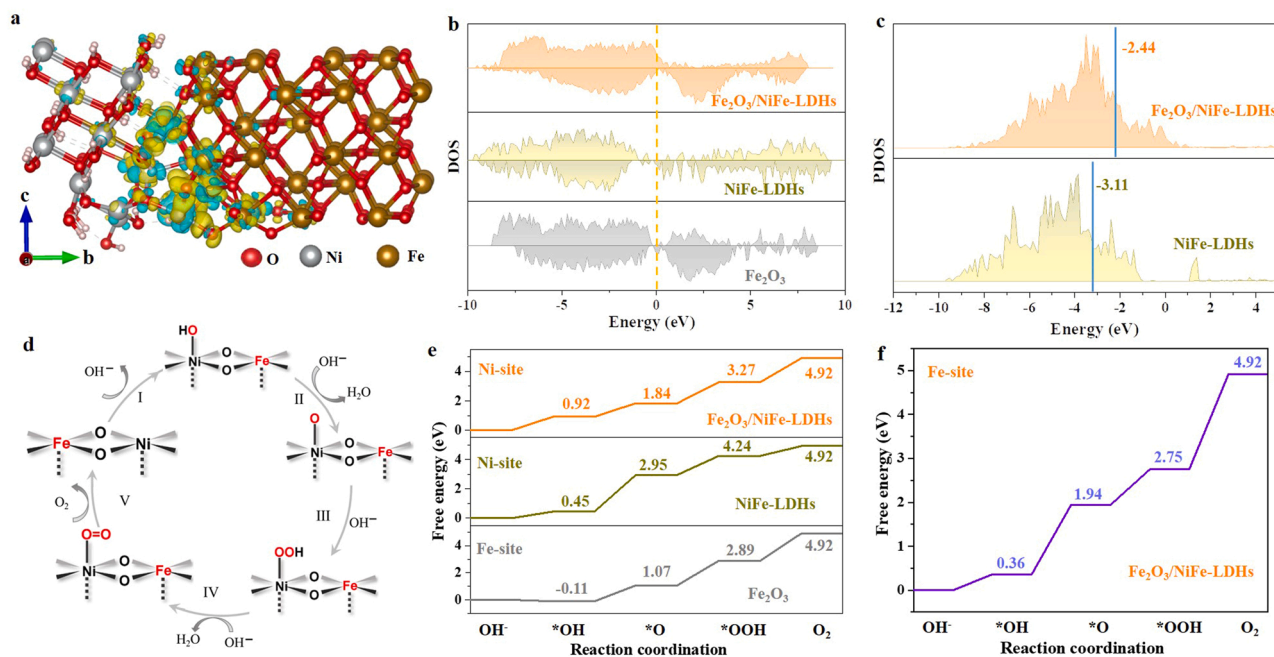


Fig. 4. a) Charge density difference of $\text{Fe}_2\text{O}_3/\text{NiFe-LDHs}$; b) Total density of states (TDOS) of Fe_2O_3 , NiFe-LDHs and $\text{Fe}_2\text{O}_3/\text{NiFe-LDHs}$; c) Projected density of states (PDOS) of NiFe-LDHs and $\text{Fe}_2\text{O}_3/\text{NiFe-LDHs}$ with d-band center; d) The detailed steps of OER on Ni active sites; e) The calculated Gibbs free energy diagrams of $\text{Fe}_2\text{O}_3/\text{NiFe-LDHs}$ (Ni site), Fe_2O_3 (Fe site) and NiFe-LDHs (Ni site); f) The calculated Gibbs free energy diagrams of $\text{Fe}_2\text{O}_3/\text{NiFe-LDHs}$ (Fe site).

To understand the benefit of charge-transfer between Ni and Fe in $\text{Fe}_2\text{O}_3/\text{NiFe-LDHs}$, we carried out the calculated charge difference between NiFe-LDHs and Fe_2O_3 samples. The corresponding theoretical models of NiFe-LDHs and $\text{Fe}_2\text{O}_3/\text{NiFe-LDHs}$ were constructed as shown in Figs. S25–S26, respectively. Notably, the strong interfacial electron redistribution occurred due to the electron transfer from Ni to Fe with 1.6 e based on Bader charge analysis (Fig. 4a), while NiFe-LDHs showed

only 1.3 e donation, indicating that more d-orbitals electrons of Ni atoms reduced significantly after introducing Fe_2O_3 , consistent with XPS results. In addition, the total density of states (TDOS) in Fig. 4b demonstrates that $\text{Fe}_2\text{O}_3/\text{NiFe-LDHs}$ shows metallic nature and owns larger density of states (DOS) near the Fermi level compared with Fe_2O_3 and NiFe-LDHs , indicating higher carrier concentration and electrical conductivity after Fe_2O_3 coupling effect [48,49]. It is well known that the

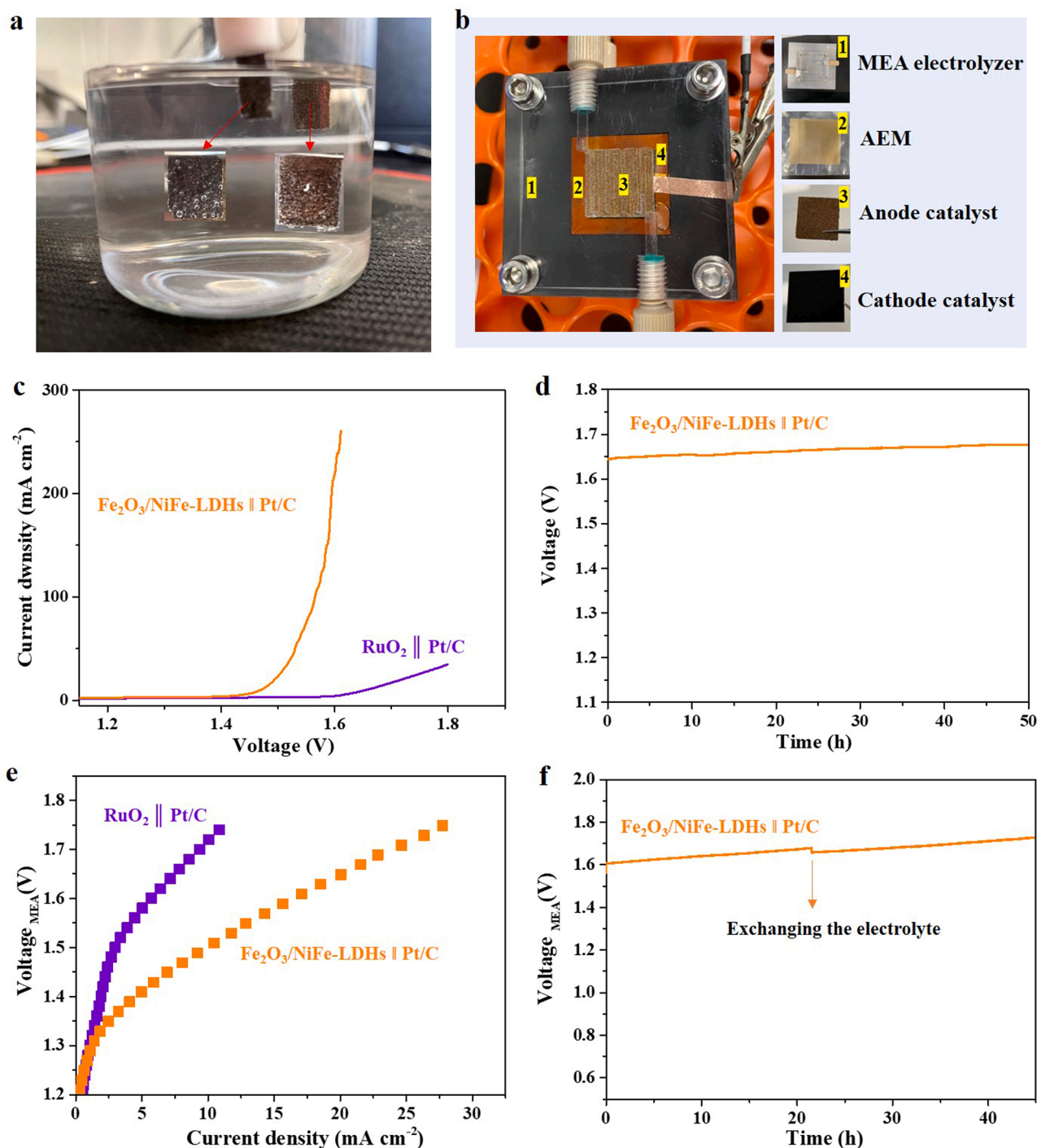


Fig. 5. a) Optical photograph of overall water splitting device of $\text{Fe}_2\text{O}_3/\text{NiFe-LDHs} \parallel \text{Pt/C}$ two-electrode electrolytic cell; b) Optical photograph of overall water splitting device of $\text{Fe}_2\text{O}_3/\text{NiFe-LDHs} \parallel \text{Pt/C}$ MEA configuration [the AEM in (b) denotes the alkaline exchange membrane]; c) iR-compensated polarization curves of $\text{Fe}_2\text{O}_3/\text{NiFe-LDHs} \parallel \text{Pt/C}$ and commercial $\text{RuO}_2 \parallel \text{Pt/C}$ for overall water splitting in two-electrode electrolytic cell; d) The long-term stability of $\text{Fe}_2\text{O}_3/\text{NiFe-LDHs} \parallel \text{Pt/C}$ at the current density of 100 mA cm^{-2} for overall water splitting in two-electrode electrolytic cell; e) iR-compensated polarization curves of $\text{Fe}_2\text{O}_3/\text{NiFe-LDHs} \parallel \text{Pt/C}$ and commercial $\text{RuO}_2 \parallel \text{Pt/C}$ for overall water splitting in MEA; f) The long-term stability of $\text{Fe}_2\text{O}_3/\text{NiFe-LDHs} \parallel \text{Pt/C}$ at the current density of 100 mA cm^{-2} for overall water splitting in MEA.

d-band center (E_d) is a valuable descriptor of the binding strength of oxygen-containing intermediates at the active sites. As shown in Fig. 4c, the projected density of states (PDOS) shows that the E_d upgrades from -3.11 eV of NiFe-LDHs to -2.44 eV of $\text{Fe}_2\text{O}_3/\text{NiFe-LDHs}$, indicating the interaction between adsorbate and catalyst surface is strengthened after the formation of $\text{Fe}_2\text{O}_3/\text{NiFe-LDHs}$ heterointerfaces. Based on the above results, the TDOS and PDOS both reveal that the introduction of Fe_2O_3 can greatly optimize the electronic structure of $\text{Fe}_2\text{O}_3/\text{NiFe-LDHs}$ to enhance OER catalytic performance.

The reaction Gibbs free energy of each step of OER is studied by DFT calculations for all samples, and the corresponding optimized geometrical structures with reaction intermediates are shown in Figs. S27–S29. The elementary periodic reaction steps consisting of the absorption, activation, reaction and desorption of oxygenated intermediates are schematically described in Fig. 4d. In the calculated free energy profiles of NiFe-LDHs and $\text{Fe}_2\text{O}_3/\text{NiFe-LDHs}$ (Fig. 4e), the rate determination step (RDS) of NiFe-LDHs is from $^*\text{OH}$ to O^* with much higher reaction free energy barrier (ΔG) of 2.5 eV, while after engineering heterointerfaces, the RDS of $\text{Fe}_2\text{O}_3/\text{NiFe-LDHs}$ is the conversion of $^*\text{OOH}$ to O_2 on the Ni site with only ΔG of 1.65 eV, indicating that the theoretical overpotential is reduced by 0.42 V after the formation of $\text{Fe}_2\text{O}_3/\text{NiFe-LDHs}$ heterointerfaces. We also investigated Fe sites at the interfaces whether are active sites as shown in Fig. 4f. Noticeably, the Fe atom sites on the interface of $\text{Fe}_2\text{O}_3/\text{NiFe-LDHs}$ exhibit higher ΔG (2.17 eV) for RDS than the Ni sites, revealing that Ni atoms is the active sites for OER, consisting with in situ Raman results.

To demonstrate the practical application ability, the catalytic performances of overall water splitting in two-electrode electrolytic cell and membrane electrode assembly (MEA) with $\text{Fe}_2\text{O}_3/\text{NiFe-LDHs}$ as anode and 20% Pt/C (1 mg/cm²) as cathode ($\text{Fe}_2\text{O}_3/\text{NiFe-LDHs} \parallel \text{Pt/C}$) were evaluated (Fig. 5a–b). For the comparison study, the noble metal-based similar electrolyzer ($\text{RuO}_2 \parallel \text{Pt/C}$) was also constructed. As shown in Fig. 5c, the $\text{Fe}_2\text{O}_3/\text{NiFe-LDHs} \parallel \text{Pt/C}$ in two-electrode electrolytic cell shows very high catalytic activity with a small cell voltage of only 1.47 at 10 mA cm^{−2}, which is much smaller than that of $\text{RuO}_2 \parallel \text{Pt/C}$ in two-electrode electrolytic cell (1.66 V). Surprisingly, even if the current density increases to 200 mA cm^{−2}, the $\text{Fe}_2\text{O}_3/\text{NiFe-LDHs} \parallel \text{Pt/C}$ two-electrode electrolytic cell still shows a small cell voltage of 1.59 V. Furthermore, the $\text{Fe}_2\text{O}_3/\text{NiFe-LDHs} \parallel \text{Pt/C}$ two-electrode electrolytic cell exhibits very high stability at a high current density of 100 mA cm^{−2} for 50 h (Fig. 5d). In order to get closer to the actual water splitting device, $\text{Fe}_2\text{O}_3/\text{NiFe-LDHs} \parallel \text{Pt/C}$ MEA configuration was constructed as shown in Fig. 5b. Obviously, the $\text{Fe}_2\text{O}_3/\text{NiFe-LDHs} \parallel \text{Pt/C}$ MEA also shows much higher catalytic activity than $\text{RuO}_2 \parallel \text{Pt/C}$ MEA for overall water splitting (Fig. 5e). Especially, the $\text{Fe}_2\text{O}_3/\text{NiFe-LDHs} \parallel \text{Pt/C}$ MEA also displays a high stability at 100 mA cm^{−2} for 50 h test as shown in Fig. 5f.

4. Conclusions

In summary, we have synthesized $\text{Fe}_2\text{O}_3/\text{NiFe-LDHs}$ with high-density heterointerfaces as catalysts for OER, and they exhibit extremely high catalytic activity under the synergistic effect between Fe_2O_3 and NiFe-LDHs. Specifically, the $\text{Fe}_2\text{O}_3/\text{NiFe-LDHs}$ achieves a low overpotential of 220 mV at a high current density of 500 mA cm^{−2} and rapid reaction kinetics with a small Tafel slope value of 32 mV dec^{−1}, indicating that $\text{Fe}_2\text{O}_3/\text{NiFe-LDHs}$ catalysts can meet the industrial-scale application. More importantly, the record high catalytic activity of $\text{Fe}_2\text{O}_3/\text{NiFe-LDHs}$ is obviously superior to that of the best NiFe LDHs catalysts reported so far. Experimental characterizations and DFT calculations reveal the reasons for remarkable performance: the interfacial Fe_2O_3 decoration can tailor Ni electronic configuration via electron transfer from Ni atoms to Fe atoms, resulting in e_g occupancy of Ni close to the unity, which will optimize the binding strength of oxygen-containing intermediates at active sites, evidenced by operando Raman and theoretical calculations. This study will facilitate the

development of high efficient catalysts with fast kinetics and will strength the understanding of interface chemistry for the design of catalysts.

CRediT authorship contribution statement

C. L. synthesized the sample and wrote the manuscript. L. X., J. Z., L. G., and J. W. carried out general characterizations. G.-R. L. provided resource, conceived the study and revised the manuscript.

Declaration of Competing Interest

The authors declare that they have no known competing financial interests or personal relationships that could have appeared to influence the work reported in this paper.

Acknowledgements

This work was supported by the National Basic Research Program of China (2016YFA0202603), NSFC (91645104, 21821003), and the Fundamental Research Funds for the Central Universities (YJ2021156).

Appendix A. Supporting information

Supplementary data associated with this article can be found in the online version at doi:10.1016/j.apcatb.2022.121097.

References

- [1] a) C.-F. Li, J.-W. Zhao, L.-J. Xie, J.-Q. Wu, G.-R. Li, Water adsorption and dissociation promoted by Co²⁺/N-C⁺-biactive sites of metallic Co/N-doped carbon hybrids for efficient hydrogen evolution, *Appl. Catal. B Environ.* 282 (2021), 119463;
b) P. Prabhu, J.-M. Lee, Metalenes as functional materials in electrocatalysis, *Chem. Soc. Rev.* 50 (2021) 6700.
- [2] a) X. Li, Y. Sun, Q. Wu, H. Liu, W. Gu, X. Wang, Z. Cheng, Z. Fu, Y. Lu, Optimized electronic configuration to improve the surface absorption and bulk conductivity for enhanced oxygen evolution reaction, *J. Am. Chem. Soc.* 141 (2019) 3121–3128;
b) H. Wang, J. Chen, Y. Lin, X. Wang, J. Li, Y. Li, L. Gao, L. Zhang, D. Chao, X. Xiao, J.-M. Lee, Electronic modulation of non-van der Waals 2D electrocatalysts for efficient energy conversion, *Adv. Mater.* 33 (2021) 2008422.
- [3] a) C.-F. Li, J.-W. Zhao, L.-J. Xie, J.-Q. Wu, G.-R. Li, Fe doping and oxygen vacancy modulated Fe-Ni₅P₄/NiFeOH nanosheets as bifunctional electrocatalysts for efficient overall water splitting, *Appl. Catal. B Environ.* 291 (2021), 119987;
b) H. Wang, J. Li, K. Li, Y. Lin, J. Chen, L. Gao, V. Nicolosi, X. Xiao, J.-M. Lee, Transition metal nitrides for electrochemical energy applications, *Chem. Soc. Rev.* 50 (2021) 1354–1390.
- [4] a) Y. Liu, Y. Ying, L. Fei, Y. Liu, Q. Hu, G. Zhang, S.Y. Pang, W. Lu, C.L. Mak, X. Luo, Valence engineering via selective atomic substitution on tetrahedral sites in spinel oxide for highly enhanced oxygen evolution catalysis, *J. Am. Chem. Soc.* 141 (2019) 8136–8145;
b) X. Hu, Y. Chen, M. Zhang, G. Fu, D. Sun, J.-M. Lee, Y. Tang, Alveolate porous carbon aerogels supported Co₉S₈ derived from a novel hybrid hydrogel for bifunctional oxygen electrocatalysis, *Carbon* 144 (2019) 557–566.
- [5] a) Y. Yang, H. Yao, Z. Yu, S.M. Islam, H. He, M. Yuan, Y. Yue, K. Xu, W. Hao, G. Sun, Hierarchical nanoassembly of MoS₂/Co₉S₈/Ni₃S₂/Ni as a highly efficient electrocatalyst for overall water splitting in a wide pH range, *J. Am. Chem. Soc.* 141 (2019) 10417–10430;
b) G. Fu, X. Yan, Y. Chen, L. Xu, D. Sun, J.-M. Lee, Y. Tang, Boosting bifunctional oxygen electrocatalysis with 3D graphene aerogel-supported Ni/MnO particles, *Adv. Mater.* 30 (2018) 1704609.
- [6] a) W. Zhang, Y. Wu, J. Qi, M. Chen, R. Cao, A thin NiFe hydroxide film formed by stepwise electrodeposition strategy with significantly improved catalytic water oxidation efficiency, *Adv. Energy Mater.* 7 (2017) 1602547;
b) G. Fu, J. Wang, Y. Chen, Y. Liu, Y. Tang, J.B. Goodenough, J.-M. Lee, Exploring indium-based ternary thiospinel as conceivable high-potential air-cathode for rechargeable Zn-air batteries, *Adv. Energy Mater.* 8 (2018) 1802263;
c) J. Chen, C. Fan, X. Hu, C. Wang, Z. Huang, G. Fu, J.-M. Lee, Y. Tang, Hierarchically porous Co/Co₃M₂ (M=P, N) as an efficient mott-schottky electrocatalyst for oxygen evolution in rechargeable Zn-air batteries, *Small* 15 (2019) 1901518.
- [7] a) F. Hu, S. Zhu, S. Chen, Y. Li, L. Ma, T. Wu, Y. Zhang, C. Wang, C. Liu, X. Yang, X. Yang, Amorphous metallic NiFeP: a conductive bulk material achieving high activity for oxygen evolution reaction in both alkaline and acidic media, *Adv. Mater.* 29 (2017) 1606570;
b) G. Fu, Y. Wang, Y. Tang, K. Zhou, J.B. Goodenough, J.-M. Lee, Superior oxygen

- electrocatalysis on nickel indium thiospinels for rechargeable Zn-air batteries, *ACS Mater. Lett.* 1 (2019) 123–131.
- [8] a) J. Xia, H. Zhao, B. Huang, L. Xu, M. Luo, J. Wang, F. Luo, Y. Du, C.H. Yan, Efficient optimization of electron/oxygen pathway by constructing ceria/hydroxide interface for highly active oxygen evolution reaction, *Adv. Funct. Mater.* 30 (2020) 1908367;
 - b) V. Jose, H. Hu, E. Edison, W.M. Jr, H. Ren, P. Kidkhunthod, S. Sreejith, A. Jayakumar, J.M.V. Nsanzimana, M.S.J. Choi, J.-M. Lee, Modulation of single atomic Co and Fe sites on hollow carbon nanospheres as oxygen electrodes for rechargeable Zn-air batteries, *Small Methods* 5 (2021) 2000751;
 - c) P. Prabhu, V. Jose, J.-M. Lee, Design strategies for development of TMD-based heterostructures in electrochemical energy systems, *Matter* 2 (2020) 526–553;
 - d) V. Jose, J.M.V. Nsanzimana, H. Hu, J. Choi, X. Wang, J.-M. Lee, Highly efficient oxygen reduction reaction activity of N-doped carbon-cobalt boride heterointerfaces, *Adv. Energy Mater.* 11 (2021) 2100157.
 - [9] J. Huang, J. Chen, T. Yao, J. He, S. Jiang, Z. Sun, Q. Liu, W. Cheng, F. Hu, Y. Jiang, CoOOH nanosheets with high mass activity for water oxidation, *Angew. Chem. Int. Ed.* 127 (2015) 8846–8851.
 - [10] Y. Zhu, H.A. Tahini, Z. Hu, Z.G. Chen, W. Zhou, A.C. Komarek, Q. Lin, H.J. Lin, C. T. Chen, Y. Zhong, Boosting oxygen evolution reaction by creating both metal ion, lattice-oxygen active sites in a complex oxide, *Adv. Mater.* 32 (2020), 1905025.
 - [11] J. Suntivich, K.J. May, H.A. Gasteiger, J.B. Goodenough, Y. Shao-Horn, A perovskite oxide optimized for oxygen evolution catalysis from molecular orbital principles, *Science* 334 (2021) 1383–1385.
 - [12] J. Guan, C. Li, J. Zhao, Y. Yang, W. Zhou, Y. Wang, Gao-Ren Li, FeOOH-enhanced bifunctionality in Ni₃N nanotube arrays for water splitting, *Appl. Catal. B Environ.* 269 (2020), 118600.
 - [13] F. Li, Y. Tian, S. Su, C. Wang, D.-S. Li, D. Cai, S. Zhang, Theoretical and experimental exploration of tri-metallic organic frameworks (t-MOFs) for efficient electrocatalytic oxygen evolution reaction, *Appl. Catal. B Environ.* 299 (2021), 120665.
 - [14] (a) G. Zhang, J. Zeng, J. Yin, C. Zuo, P. Wen, H. Chen, Y. Qiu, Iron-facilitated surface reconstruction to in-situ generate nickel-iron oxyhydroxide on self-supported FeNi alloy fiber paper for efficient oxygen evolution reaction, *Appl. Catal. B Environ.* 286 (2021), 119902;
 - (b) J.A.D. Rosario, G. Li, M.F.M. Labata, D. Joey, P.Y.A. Ocon, Chuang, Unravelling the roles of alkali-metal cations for the enhanced oxygen evolution reaction in alkaline media, *Appl. Catal. B Environ.* 288 (2021), 119981.
 - [15] (a) H. Zeng, M. Oubla, X. Zhong, N. Alonso-Vante, F. Duc, Y. Xie, Y. Huang, J. Ma, Rational defect and anion chemistries in Co₃O₄ for enhanced oxygen evolution reaction, *Appl. Catal. B Environ.* 281 (2021), 119535;
 - (b) C. Chen, Y. Tuo, Q. Lu, H. Lu, S. Zhang, Y. Zhou, J. Zhang, Z. Liu, Z. Kang, X. Feng, D. Chen, Hierarchical trimetallic Co-Ni-Fe oxides derived from core-shell structured metal-organic frameworks for highly efficient oxygen evolution reaction, *Appl. Catal. B Environ.* 287 (2021), 119953.
 - [16] L. Sun, Z. Dai, L. Zhong, Y. Zhao, Y. Cheng, S. Chong, G. Chen, C. Yan, X. Zhang, H. Tan, L. Zhang, K.N. Dinh, S. Li, F. Ma, Q. Yan, Lattice strain and atomic replacement of CoO₆ octahedra in layered sodium cobalt oxide for boosted water oxidation electrocatalysis, *Appl. Catal. B Environ.* 297 (2021), 120477.
 - [17] Y. Zhang, H. Guo, J. Ren, X. Li, W. Ren, R. Song, MoO₃ crystal facets modulation by doping heteroatom Fe from polyoxometalate for quasi-industrial oxygen evolution reaction, *Appl. Catal. B Environ.* 298 (2021), 120582.
 - [18] J. Jiang, F. Sun, S. Zhou, W. Hu, H. Zhang, J. Dong, Z. Jiang, J. Zhao, J. Li, W. Yan, Atomic-level insight into super-efficient electrocatalytic oxygen evolution on iron and vanadium co-doped nickel (oxy)hydroxide, *Nat. Commun.* 9 (2018) 1–12.
 - [19] J. Li, D. Chu, H. Dong, D.R. Baker, R. Jiang, Boosted oxygen evolution reactivity by igniting double exchange interaction in spinel oxides, *J. Am. Chem. Soc.* 142 (2019) 50–54.
 - [20] X. Zheng, B. Zhang, P. De Luna, Y. Liang, R. Comin, O. Voznyy, L. Han, F.P.G. De Arquer, M. Liu, C.T. Dinh, Theory-driven design of high-valence metal sites for water oxidation confirmed using in situ soft X-ray absorption, *Nat. Chem.* 10 (2018) 149–154.
 - [21] W. Guo, D. Li, D. Zhong, S. Chen, G. Hao, G. Liu, J. Li, Q. Zhao, Loading FeOOH on Ni(OH)₂ hollow nanorods to obtain a three-dimensional sandwich catalyst with strong electron interactions for an efficient oxygen evolution reaction, *Nanoscale* 12 (2020) 983–990.
 - [22] L. Bai, S. Lee, X. Hu, Spectroscopic and electrokinetic evidence for a bifunctional mechanism of the oxygen evolution reaction, *Angew. Chem. Int. Ed.* 133 (2021) 3132–3140.
 - [23] G. Kresse, J. Furthmüller, Efficient iterative schemes for ab initio total-energy calculations using a plane-wave basis, *Phys. Rev. B* 54 (1996) 11169–11186.
 - [24] J.P. Perdew, K. Burke, M. Ernzerhof, Generalized gradient approximation made simple, *Phys. Rev. Lett.* 77 (1996) 3865–3868.
 - [25] G. Kresse, D. Joubert, From ultrasoft pseudopotentials to the projector augmented-wave method, *Phys. Rev. B* 59 (1999) 1758–1775.
 - [26] P.E. Blochl, Projector augmented-wave method, *Phys. Rev. B* 50 (1994) 17953–17979.
 - [27] S. Grimme, J. Antony, S. Ehrlich, H.J. Krieg, A consistent and accurate ab initio parametrization of density functional dispersion correction (DFT-D) for the 94 elements H-Pu, *J. Chem. Phys.* 132 (2010), 154104.
 - [28] G. Henkelman, B.P. Uberuaga, H.J. Jonsson, A climbing image nudged elastic band method for finding saddle points and minimum energy paths, *J. Chem. Phys.* 113 (2000) 9901–9904.
 - [29] Z. Lu, W. Zhu, X. Yu, H. Zhang, Y. Li, X. Sun, X. Wang, H. Wang, J. Wang, J. Luo, Ultrahigh hydrogen evolution performance of under-water “superaerophobic” MoS₂ nanostructured electrodes, *Adv. Mater.* 26 (2014) 2683–2687.
 - [30] J. Wang, Q. Yang, M. Wang, C. Wang, L. Jiang, Rose petals with a novel and steady Air bubble pinning effect in aqueous media, *Soft Matter* 8 (2012) 2261–2266.
 - [31] M.W. Louie, A.T. Bell, An investigation of thin-film Ni-Fe oxide catalysts for the electrochemical evolution of oxygen, *J. Am. Chem. Soc.* 135 (2013) 12329–12337.
 - [32] C. Baratto, P. Lottici, D. Bersani, G. Antonioli, G. Gnappi, A. Montenero, Sol-gel preparation of α -Fe₂O₃ thin films: structural characterization by XAFS and raman, *J. Sol Gel Sci. Technol.* 13 (1998) 667–671.
 - [33] F. Bao, J.-L. Yao, R.-A. Gu, Synthesis of magnetic Fe₂O₃/Au core/shell nanoparticles for bioseparation and immunoassay based on surface-enhanced raman spectroscopy, *Langmuir* 25 (2009) 10782–10787.
 - [34] I. Dincer, C. Acar, Int. Review and evaluation of hydrogen production methods for better sustainability, *Int. J. Hydrog. Energy* 40 (2015) 11094–11111.
 - [35] X.L. Shao, J.S. Zhao, K.L. Zhang, R. Chen, K. Sun, C.J. Chen, K. Liu, L.W. Zhou, J. Y. Wang, C.M. Ma, Two-step reset in the resistance switching of the Al/TiO_x/Cu structure, *ACS Appl. Mater. Interfaces* 5 (2013) 11265–11270.
 - [36] X. Zhao, H. Su, W. Cheng, H. Zhang, W. Che, F. Tang, Q. Liu, Operando insight into the oxygen evolution kinetics on the metal-free carbon-based electrocatalyst in an acidic solution, *ACS Appl. Mater. Interfaces* 11 (2019) 34854–34861.
 - [37] A. Dutta, S. Mutyal, A.K. Samantara, S. Bera, B.K. Jena, N. Pradhan, Synergistic effect of inactive iron oxide core on active nickel phosphide shell for significant enhancement in oxygen evolution reaction activity, *ACS Energy Lett.* 3 (2017) 141–148.
 - [38] L. Yu, H. Zhou, J. Sun, F. Qin, F. Yu, J. Bao, Y. Yu, S. Chen, Z. Ren, Cu nanowires shelled with NiFe layered double hydroxide nanosheets as bifunctional electrocatalysts for overall water splitting, *Energy Environ. Sci.* 10 (2017) 1820–1827.
 - [39] T. Bao, L. Song, S. Zhang, Synthesis of carbon quantum dot-doped NiCoP and enhanced electrocatalytic hydrogen evolution ability and mechanism, *Chem. Eng. J.* 351 (2018) 189–194.
 - [40] A.T. Swesi, J. Masud, W.P. Liyanage, S. Umapathi, E. Bohannan, J. Medvedeva, M. Nath, Textured NiSe₂ film: bifunctional electrocatalyst for full water splitting at remarkably low overpotential with high energy efficiency, *Sci. Rep.* 7 (2017) 1–11.
 - [41] Y. Wang, S. Tao, H. Lin, S. Han, W. Zhong, Y. Xie, J. Hu, S. Yang, NaBH₄ induces a high ratio of Ni³⁺/Ni²⁺ boosting OER activity of the NiFe LDH electrocatalyst, *RSC Adv.* 10 (2020) 33475–33482.
 - [42] H. Shin, H. Xiao, W.A. Goddard III, In silico discovery of new dopants for Fe-doped Ni oxyhydroxide (Ni_{1-x}Fe_xOOH) catalysts for oxygen evolution reaction, *J. Am. Chem. Soc.* 140 (2018) 6745–6748.
 - [43] L. Zhuang, L. Ge, H. Liu, Z. Jiang, Y. Jia, Z. Li, D. Yang, R.K. Hocking, M. Li, L. Zhang, A Surfactant-free and scalable general strategy for synthesizing ultrathin two-dimensional metal-organic framework nanosheets for the oxygen evolution reaction, *Angew. Chem. Int. Ed.* 131 (2019) 13699–13706.
 - [44] H.Y. Wang, Y.Y. Hsu, R. Chen, T.S. Chan, H.M. Chen, B. Liu, Ni³⁺-induced formation of active NiOOH on the spinel Ni-Co oxide surface for efficient oxygen evolution reaction, *Adv. Energy Mater.* 5 (2015), 1500091.
 - [45] J.-C. Dong, M. Su, V. Briega-Martos, L. Li, J.-B. Le, P. Radjenovic, X.-S. Zhou, J. M. Feliu, Z.-Q. Tian, J.-F. Li, Direct in situ raman spectroscopic evidence of oxygen reduction reaction intermediates at high-index Pt (hkl) Surfaces, *J. Am. Chem. Soc.* 142 (2019) 715–719.
 - [46] J. Xing, K. Guo, Z. Zou, M. Cai, J. Du, C. Xu, In situ growth of well-ordered NiFe-MOF-74 on Ni foam by Fe²⁺ induction as an efficient and stable electrocatalyst for water oxidation, *Chem. Commun.* 54 (2018) 7046–7049.
 - [47] X. Bo, R.K. Hocking, S. Zhou, Y. Li, X. Chen, J. Zhuang, Y. Du, C. Zhao, Capturing the active sites of multimetallic (oxy)hydroxides for the oxygen evolution reaction, *Energy Environ. Sci.* 13 (2020) 4225–4237.
 - [48] P. Yan, Q. Liu, H. Zhang, L. Qiu, H.B. Wu, X.-Y. Yu, Deeply reconstructed hierarchical and defective NiOOH/FeOOH nanoboxes with accelerated kinetics for oxygen evolution reaction, *J. Mater. Chem. A* 9 (2021) 15586–15594.
 - [49] K. Lu, G. Chang, H. Zhang, X.-Y. Yu, Accelerating the oxygen evolution reaction kinetics of Co₃O₄ in neutral electrolyte by decorating RuO₂, *Chem. Commun.* 57 (2021) 2907–2910.